Anomalous fluctuations in homogeneous fluid phase of active Brownian particles

Yuta Kuroda ⬤,[*] Hiromichi Matsuyama, Takeshi Kawasaki ⬤, and Kunimasa Miyazaki ⬤[†]

Department of Physics, Nagoya University, Nagoya 464-8602, Japan

Giant number fluctuations (GNF) are an anomaly universally observed in active fluids with polar or nematic order. In this paper, we show that GNF arise in the fluid phase of active Brownian particles (ABP), where the polar order is absent. GNF in ABP extends over a large but finite length which characterizes the growing velocity correlations. To suppress unwanted phase separation and allow ones to explore the disordered fluid phase at large activities, we impart the inertia, or the mass, to the ABP. A linearized hydrodynamic theory captures our findings, but only qualitatively. We find numerically a nontrivial scaling relation for the density correlation function, which the linearized theory cannot explain. The results suggest ubiquitousness of the anomalous fluctuations even in the disordered homogeneous fluid phase in the absence of the directional order.

I. INTRODUCTION

Active matter refers to a broad class of many-body systems consisting of self-propelling constituents, such as flocks of birds, herds of animals, bacterial colonies, or even self-propelled colloidal particles [1–3]. In the past few decades, we have witnessed tremendous progress in the studies of active matter. Active matter systems exhibit many nontrivial phenomena that are prohibited in equilibrium systems. Representative examples include anomalous increases of particle number fluctuations known as giant number fluctuations (GNF) [4–6], spatiotemporal chaotic patterns of velocities fields reminiscent of turbulence [7,8], and spontaneous separation of constituent particles into dense and dilute phases called the motility-induced phase separation (MIPS) [9,10].

The active Brownian particles (ABP) model is one of the simplest models of active matter [10] and has been used to study MIPS theoretically [11–19] and numerically [10,20–26]. MIPS resembles the liquid-vapor phase separation in equilibrium systems, and some efforts were made to understand MIPS by mapping ABP and other active fluids into the effective equilibrium system [13,16,17,27–29]. Recently, however, it has been realized that MIPS of ABP is accompanied by intrinsically nonequilibrium phenomena, such as negative surface tension [28,30], reversal of the Ostwald process [31,32], and spatial velocity correlation [33]. In particular, the spatial velocity correlation is not only observed inside the MIPS phase but also in the high-density regimes, including the crystalline [34,35], amorphous [36,37], and even

dense fluid phases [34,38,39]. The spatial velocity correlation is manifested as the vortex-shaped patterns, which suggests a deep connection with the active turbulence [39].

Since the longitudinal part of the velocity field is directly related to the density field, it is natural to expect that the growth of the velocity correlation leads to an increase of the density fluctuations similar to GNF in the ordered phase of polar active fluids [2,40–42]. If such large density fluctuations exist in ABP fluids, it is tempting to see the connection between them and GNF observed in the systems with polar long-range order. Several studies have reported large number fluctuations in ABP [10,21,25], but it is difficult to judge whether the observed data are due to *bona fide* GNF or originated from heterogeneities by MIPS.

In this paper, we demonstrate that the homogeneous fluid state of ABP, despite the absence of the polar or nematic order, develops the large density fluctuations and GNF, whose sizes increase with the growing spatial correlation of the longitudinal velocity. The main obstacle to observing number fluctuations is heterogeneous density modulation caused by MIPS at high activity. One way to avoid MIPS is to explore the high-density region [34,38,39], but the glassy slow dynamics or the precursor of crystallization would intervene there. Another route is to study the intermediate-density fluid phase outside the binodal region. However, the activity is too low to observe any meaningful signal of the growing fluctuations. To overcome these practical issues, we consider ABP with the inertia term or the mass. It is known that MIPS is suppressed if the inertia term is added to the original overdamped ABP [43]. If the mass is sufficiently large, then the system remains homogeneous without a sign of phase separation even at high activity. It enables one to investigate intrinsically nonequilibrium fluctuations without being impeded by unwanted MIPS.

We confirm numerically that the spatial velocity correlation develops even at intermediate densities. Their longitudinal and transverse modes are characterized by two distinct correlation lengths, as reported in the high-density fluid state [38]. The transverse velocity correlation is associated with the

---

*kuroda@r.phys.nagoya-u.ac.jp
†miyazaki@r.phys.nagoya-u.ac.jp

vortex structure, reminiscent of active turbulence [39], whereas the longitudinal one is accompanied by the spatial correlation of the density fluctuations. The correlation lengths of the longitudinal velocity and density increase with the activity. This results in the emergence of GNF. Contrary to the case of polar fluids where GNF arise due to the polar order [2,40–42], GNF in ABP are confined in a large but finite length scale corresponding to longitudinal correlation length. We develop a linearized fluctuating hydrodynamic theory from the microscopic model and show that the growing lengths and GNF can be qualitatively captured by the linearized theory. The theory clarifies the similarities and differences of the mechanism of GNF between our system and the polar active fluids in the ordered phase [2,4,40,41]. However, the linearized theory fails to explain the nontrivial scaling relation and scaling exponents shown by the simulation. This implies that the nonlinear coupling of fluctuations is at play.

This paper is organized as follows. In Sec. II, we describe the model and simulation setting. Numerical results are shown in Sec. III. The analysis based on the linearized hydrodynamic theory is sketched in Sec. IV. We devote Sec. V to a summary.

II. MODEL AND SIMULATION SETTING

We consider two-dimensional active Brownian particles with a finite mass, which we refer to as the inertial active Brownian particles (iABP). The Langevin equation which iABP obey is written as

$$m\frac{d^2\boldsymbol{r}_j(t)}{dt^2} = -\zeta\frac{d\boldsymbol{r}_j(t)}{dt} - \nabla_j\sum_{k<l}U(r_{kl}) + \zeta v_0\boldsymbol{e}(\phi_j), \quad (1)$$

where $\boldsymbol{r}_j$ is the position of the jth particle, m is the mass of a particle, ζ is the friction coefficient, $U(r_{kl})$ is the pairwise interaction potential between the particles k and l, $r_{kl} = |\boldsymbol{r}_k - \boldsymbol{r}_l|$ is the distance between the two particles, and ∇_j denotes the gradient acting on $\boldsymbol{r}_j$. The last term of the right-hand side of Eq. (1) is the active noise. Its strength is characterized by the self-propelling speed v_0, and the direction is represented by a unit vector $\boldsymbol{e}(\phi_j) = (\cos\phi_j, \sin\phi_j)$. The dynamics of orientation ϕ_j of the particle j is described by

$$\frac{d\phi_j(t)}{dt} = \sqrt{\frac{2}{\tau_p}}\eta_j(t), \quad (2)$$

where $\eta_j(t)$ is the Gaussian white noise that satisfies $\langle\eta_j(t)\rangle = 0$ and $\langle\eta_j(t)\eta_k(t')\rangle = \delta_{j,k}\delta(t - t')$. The symbol $\langle\cdots\rangle$ denotes the ensemble average, and τ_p is the persistence time, an essential parameter characterizing how far the system is from equilibrium. In the $\tau_p \to 0$ limit, Eq. (1) becomes the equilibrium Langevin equation with the effective temperature $T_{\text{eff}} = v_0^2\tau_p\zeta/2$. Mandal *et al.* [43] employed the iABP with both the translational thermal noise and the rotational inertial term for ϕ_j, which we do not consider here for simplicity.

The simulation setting is as follows. We employ the Weeks-Chandler-Andersen potential as a pairwise potential [44]:

$$U(r_{kl}) = 4\epsilon\left\{\left(\frac{\sigma}{r_{kl}}\right)^{12} - \left(\frac{\sigma}{r_{kl}}\right)^6 + \frac{1}{4}\right\}\theta(2^{1/6}\sigma - r_{kl}), \quad (3)$$

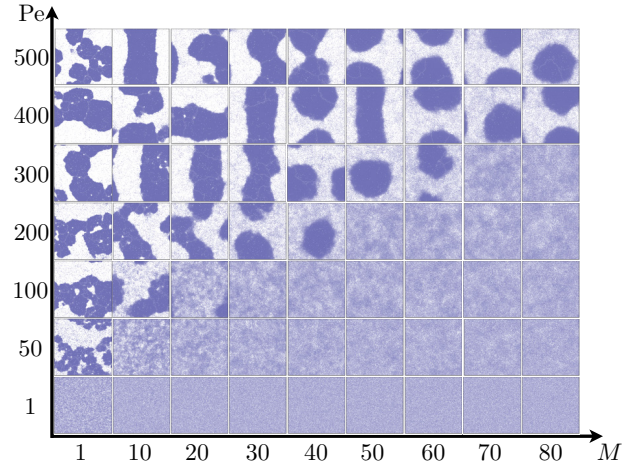FIG. 1. Snapshots of particle configurations in (M, Pe) space; $\rho = 0.5$ and $N = 4 \times 10^4$. MIPS is suppressed as M increases. In this study, we focus on the region $M = 80$, $\text{Pe} \leqslant 200$.

where $\theta(x)$ is the Heaviside step function and σ is the diameter of a particle. We choose $\tau_v = \sigma/v_0$ and σ as the units of time and length, respectively. The number density is set relatively low at $\rho = 0.5$, and the system size is $L = \sqrt{N/\rho}$. Control parameters in the simulation are the Péclet number defined by $\text{Pe} = \tau_p/\tau_v = \tau_p v_0/\sigma$, the dimensionless mass $M = m/(\zeta\tau_v)$, and the energy ratio $\epsilon/(\zeta v_0\sigma)$. Here we set $\epsilon/(\zeta v_0\sigma) = 100$. We carry out the Brownian dynamics simulation for iABP with the periodic boundary condition. To integrate the equation of motion, we use the Euler-Maruyama method with a time step $\Delta t = 10^{-2}\tau_v$. The number of particles $N = 1 \times 10^4$, 4×10^4, and 1×10^5 are chosen to check the system size effect. For the computation of the correlation functions discussed below, we take the time average after confirming that the system is sufficiently relaxed to the stationary state by monitoring the time evolution of the potential energy.

III. NUMERICAL RESULTS

Figure 1 shows snapshots of particle configurations in (M, Pe) space. At $M = 1$, the inertia effect is negligible, and the system undergoes MIPS at $\text{Pe} \gtrsim 50$, as reported for the overdamped ABP [10,20,25]. As M increases, the MIPS phase boundary line shifts to a larger Pe continuously, and at the largest $M \simeq 80$, the system remains in the homogeneous fluid phase even at $\text{Pe} = 300$ (see also Appendix A for the system size dependence). Now that we successfully generated a homogeneous fluid with large Péclet numbers, we explore the properties of nonequilibrium fluctuations of ABP without being intervened by unwanted inhomogeneity induced by MIPS.

Figure 2 presents typical snapshots of the density field $\rho(\boldsymbol{r})$ [Figs. 2(a)–2(c)], velocity field $\boldsymbol{v}(\boldsymbol{r})$ [Figs. 2(d)–2(f)], and vorticity field $\Omega(\boldsymbol{r}) = [\nabla \times \boldsymbol{v}(\boldsymbol{r})]_z$ [Figs. 2(g)–2(i)] for $\text{Pe} = 1, 50$, and 200 at $M = 80$ (see Appendix B for the computation method). First, we focus on the velocity and vorticity fields. The colors in Figs. 2(d)–2(f) represent the angle of vector $\boldsymbol{v}(\boldsymbol{r})$ with respect to the x axis. The velocity pattern is uniform for $\text{Pe} = 1$, where the system is close
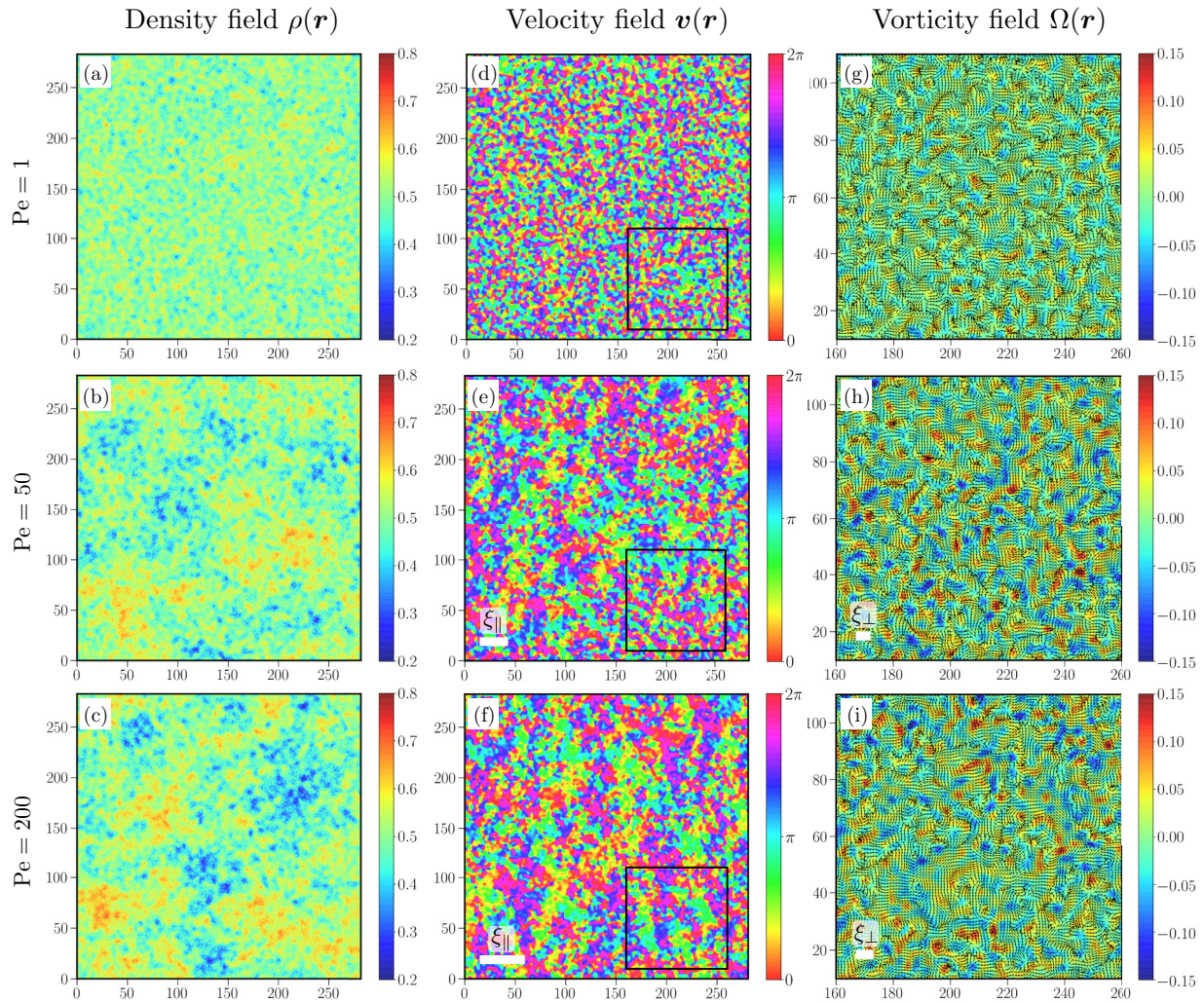
FIG. 2. Snapshots of density [(a)–(c)], velocity [(d)–(f)], and vorticity fields [(g)–(i)] for Pe = 1, 50, 200 at $M = 80$. Number of particles is $N = 4 \times 10^4$. The horizontal and vertical axes denote the x and y coordinates, respectively. Small boxes in panels (d)–(f) correspond to the plot range of panels (g)–(i), respectively. The colors represent the local density in panels (a)–(c), the angle of local velocity with respect to the x axis in panels (d)–(f), and the local vorticity in panels (g)–(i), respectively. Black arrows in panels (g)–(i) represent the direction of local velocity. The horizontal white scale bars in panels (e), (f), (h), and (i) denote the longitudinal and transverse correlation lengths obtained by the velocity correlation functions (see the text).

to equilibrium. As Pe increases, velocity-aligned domains appear and their sizes grow. Concomitantly, the vorticity field $\Omega(\boldsymbol{r})$ develops as shown in Figs 2(g)–2(i). The sizes of the patterns, however, are appreciably smaller than those of $\boldsymbol{v}(\boldsymbol{r})$. To quantify these spatial patterns, we define the longitudinal and transverse velocity correlation functions in the Fourier space by [38]

$$\omega_\parallel(q) = \frac{1}{N}\langle |J_\parallel(\boldsymbol{q})|^2\rangle, \quad \omega_\perp(q) = \frac{1}{N}\langle |J_\perp(\boldsymbol{q})|^2\rangle. \quad (4)$$

Here we decomposed the Fourier transformed current $\boldsymbol{J}(\boldsymbol{q}) = \sum_j \dot{\boldsymbol{r}}_j e^{-i\boldsymbol{q}\cdot\boldsymbol{r}_j}$ as $\boldsymbol{J}(\boldsymbol{q}) = J_\parallel(\boldsymbol{q})\hat{\boldsymbol{q}}_\parallel + J_\perp(\boldsymbol{q})\hat{\boldsymbol{q}}_\perp$; $\hat{\boldsymbol{q}}_\parallel$ and $\hat{\boldsymbol{q}}_\perp$ denote the unit vector parallel and perpendicular to the wave vector $\boldsymbol{q}$, respectively. As we can directly derive from Eq. (1), both $\omega_\parallel(q)$ and $\omega_\perp(q)$ take the value $\omega_0 = \text{Pe}/[2(M + \text{Pe})]$ at $q = 0$. This value is used for the fitting to evaluate correlation lengths discussed below. $\omega_\parallel(q)$ is a good measure to probe the extent of the alignment of the velocity of particles, whereas

$\omega_\perp(q)$ probes the development of the vorticity pattern. Figures 3(a) and 3(b) show the q dependence of $\omega_\parallel(q)$ and $\omega_\perp(q)$ for various Pe at $M = 80$ (see Appendix E for ρ dependence). Both $\omega_\parallel(q)$ and $\omega_\perp(q)$ grow significantly at small wave number. This behavior indicates the development of the spatial correlations of both the longitudinal and transverse velocities. We extract correlation lengths by fitting with the Ornstein-Zernike function $\omega_\mu(q) = \omega_0/[1 + (\xi_\mu q)^2]$, ($\mu = \parallel, \perp$), for the two correlation functions [see the insets of Figs. 3(a) and 3(b)] [38]. The fitting range is $q < 0.06$ for $\omega_\parallel(q)$ and $q < 0.3$ for $\omega_\perp(q)$. Figure 3(c) shows the correlation length obtained by fitting for Pe $\geqslant 10$. We left out the data for Pe = 1 because the data are too small to extract the correlation length. We find that the two correlation lengths are distinct; the longitudinal length $\xi_\parallel$ is much longer than the transverse counterpart $\xi_\perp$, and $\xi_\parallel$ grows with Pe, whereas the dependence of $\xi_\perp$ on Pe is much weaker, which is again consistent with the results in Ref. [38]. $\xi_\parallel$ and $\xi_\perp$ are comparable to the sizes of patterns
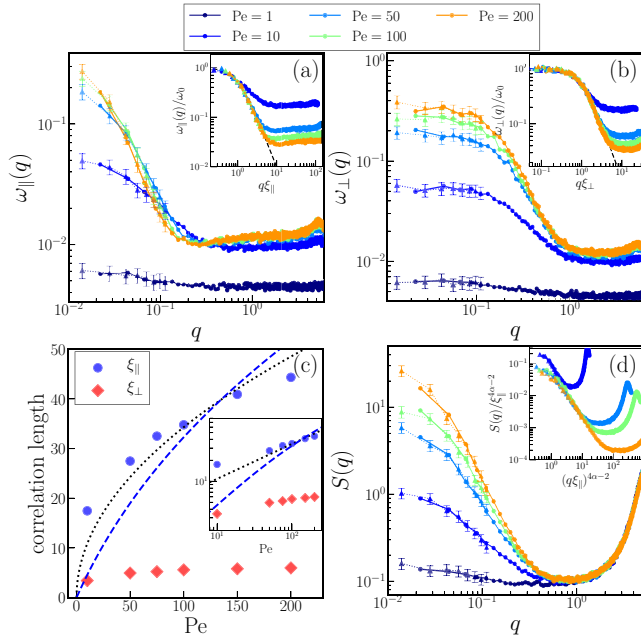
FIG. 3. The velocity correlation functions and static structure factor at $M = 80$ in the Fourier space. (a) The longitudinal, (b) transverse part of the velocity correlation functions, and (d) the static structure factor. Filled circles and triangles represent data for $N = 4 \times 10^4$ and $N = 1 \times 10^5$, respectively. The latter data are depicted with standard error. The insets of panels (a) and (b) are the fits by the Ornstein-Zernike function (the dashed line). (c) The longitudinal and transverse correlation lengths $\xi_\parallel$ and $\xi_\perp$ obtained by the fitting as a function of the Péclet number. The dotted line is the fit by $\xi_\parallel \propto \mathrm{Pe}^{1/2}$, and the blue dashed line is the fit by the linearized hydrodynamic theory (see Sec. IV). The inset is the log-log plot of the same data. The inset of panel (d) is the rescaled curves of $S(q)$ by $\xi_\parallel$ and α (see the text).
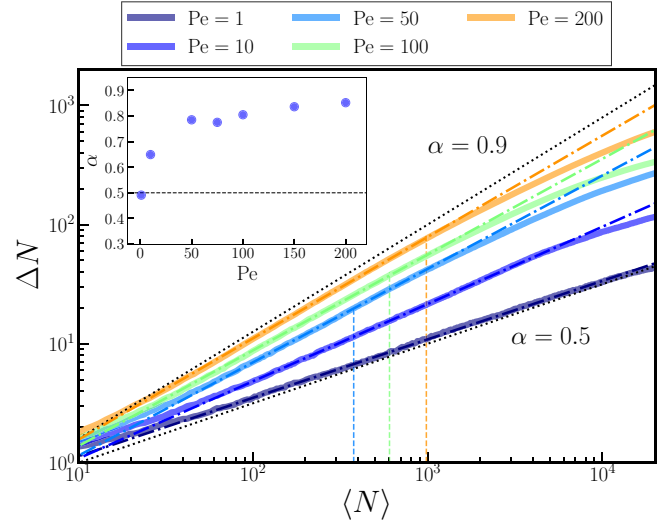

FIG. 4. Number fluctuation ΔN as a function of $\langle N \rangle$ at $M = 80$. The solid and dot-dashed lines are simulation data and power-law fits, respectively. The dotted lines indicate $\langle N \rangle^\alpha$ with $\alpha = 0.5$ and 0.9 shown as a guide to the eye. The vertical dashed lines represent the value of $\langle N \rangle$ at $\ell = \xi_\parallel$. The dependence of the exponent α on Pe is plotted in the inset.

of the velocity and the vorticity shown in Figs 2(e), 2(f) 2(h), and 2(i). These observations are qualitatively consistent with the numerical results by Szamel and Flenner [38] and the prediction of the linearized fluctuating hydrodynamic theory by Marconi *et al.* [45]. Note that large spatial velocity correlations can be confirmed in real space, as reported in Refs. [34,35]. The thus-obtained correlation length is close to the value of $\xi_\perp$ (see Appendix C). This is natural, as $\xi_\perp$ is smaller than $\xi_\parallel$. The vortex pattern in Figs. 2(h) and 2(i) and the bahavior of $\omega_\perp(q)$ at high Pe are reminiscent of the active turbulence reported in various active matter systems [7,8,46–54]. We find that the energy spectrum $E(q)$ obtained from the velocity correlation function $\omega(q) = \omega_\parallel(q) + \omega_\perp(q)$ exhibits weak power-law behavior (see Appendix D). However, the power-law exponent of $E(q)$ is small compared with those reported in other studies [7,8,46–54]. Seeking a link between the active turbulence and the observed spatial correlation is out of the scope of the present study and is left for future work.

In Fig. 3(d), we show the density correlation function, or the static structure factor, defined by $S(q) = \langle \delta\rho(\boldsymbol{q}) \delta\rho(-\boldsymbol{q}) \rangle / N$, where $\delta\rho(\boldsymbol{q}) = \rho(\boldsymbol{q}) - \langle \rho(\boldsymbol{q}) \rangle$ is the fluctuations of the Fourier transformed density field $\rho(\boldsymbol{q}) =$ $\sum_j e^{-i\boldsymbol{q} \cdot \boldsymbol{r}_j}$. $S(q)$ at small wave number is almost constant at $\mathrm{Pe} = 1$ but rises significantly as Pe increases, meaning that the density fluctuations increase at large scales. Note that the increase of $S(q)$ at small wave numbers is distinct from that observed in the MIPS phase (see Appendix F). In the latter case, $S(q)$ is well fitted by $q^{-(d+1)}$ (d is the spatial dimension), which is called Porod's law [55,56], and it is a natural consequence of the domains created by the phase separation. On the contrary, the system in our study is spatially uniform and the increase of $S(q)$ observed in Fig. 3(d) is induced by the large correlation of the longitudinal velocity field.

Finally, we investigate the particle number fluctuations defined by $\Delta N = \sqrt{\langle (N - \langle N \rangle)^2 \rangle}$. We measure ΔN and the average number of particles $\langle N \rangle$ in the sub-box with the side length ℓ ($< L$) in the whole system. In equilibrium systems, ΔN should be proportional to $\langle N \rangle^{1/2}$. In active matter with polar or nematic order, however, GNF characterized by $\Delta N \propto \langle N \rangle^\alpha$ with a larger exponent $\alpha > 0.5$ are observed [5,6,42,57–64]. The iABP model is ideal for examining GNF because MIPS is absent even at large Péclet numbers. In Fig. 4, we plot ΔN as a function of $\langle N \rangle$ for several Pe for a fixed $M (= 80)$. ΔN behaves as $\langle N \rangle^\alpha$ with exponent $\alpha > 0.5$ for large Pe. We chose the fitting range as $\langle N \rangle \in [100, 1000]$ to extract the exponent α. The dot-dashed lines in Fig. 4 are the power-law fit of the simulation data. Interestingly, the side length ℓ at which ΔN deviates from the power law is comparable to $\xi_\parallel$, as indicated by vertical dashed lines in Fig. 4. The dependence of the exponent α on Pe is plotted in the inset of Fig. 4. Starting from the smallest value of $\alpha \simeq 0.5$ at $\mathrm{Pe} = 1$, α increases with Pe, up to $\alpha \simeq 0.85$ at the largest Pe.

The number fluctuation ΔN is related to the static structure factor $S(q)$ by $S(q \to 0) = \Delta N^2 / \langle N \rangle$ at large ℓ. Therefore, $\Delta N \propto \langle N \rangle^\alpha$ leads to $S(q) \propto q^{-\beta}$ in the reciprocal space. The two exponents are related by $\beta = 4\alpha - 2$ [4,65]. On the other

hand, it is natural to expect that the density fluctuations are characterized by the correlation length of the longitudinal velocity correlation function, $\xi_\parallel$. Thus, we assume the scaling form

$$S(q) = \xi_\parallel^\beta f(q\xi_\parallel), \tag{5}$$

where the scaling function satisfies $f(x) \sim$ const for $x < 1$ and $f(x) \sim x^{-\beta}$ for $x > 1$. The inset of Fig. 3(d) is the rescaled plot of $S(q)$ for Pe $\geqslant 10$. The data collapse to a single curve for Pe $\geqslant 50$, but the data for Pe $= 10$ deviate from the curve. This supports the validity of the scaling ansatz at least for Pe $\geqslant 50$ and confirms the relation between GNF and $S(q)$.

IV. QUALITATIVE DESCRIPTION OF GIANT NUMBER FLUCTUATIONS

To explain the connection between the velocity correlation and GNF observed above, here we develop a linearized fluctuating hydrodynamic theory for the homogeneous fluid state of iABP. For active fluids with polar or nematic order, the linearized hydrodynamics explain GNF as a result of coupling between the density field and order parameter, which is prohibited in equilibrium systems [2,4,41]. GNF in the fluid state of iABP, where the order or Goldstone modes are absent, arise by a similar but different mechanism. In this section, we sketch their derivation. Following Dean's method [66,67] and assuming that the interaction term (pressure gradient) linearly depends only on the density, we can derive the linearized equation for the density, current, and polarization fields from Eqs. (1) and (2) (see Appendix G for derivation):

$$\partial_t \delta\rho(\mathbf{r}, t) = -\nabla \cdot \delta\mathbf{J}(\mathbf{r}, t),$$

$$m\partial_t \delta\mathbf{J}(\mathbf{r}, t) = -\frac{1}{\rho\chi}\nabla\delta\rho(\mathbf{r}, t) - \zeta\delta\mathbf{J}(\mathbf{r}, t) + \zeta v_0 \delta\mathbf{p}(\mathbf{r}, t),$$

$$\partial_t \delta\mathbf{p}(\mathbf{r}, t) = -\frac{1}{\tau_p}\delta\mathbf{p}(\mathbf{r}, t) + \sqrt{\frac{\rho}{\tau_p}}\mathbf{\Upsilon}(\mathbf{r}, t), \tag{6}$$

where $\mathbf{p}(\mathbf{r}, t) = \sum_{j=1}^N \mathbf{e}[\phi_j(t)]\delta[\mathbf{r} - \mathbf{r}_j(t)]$ denotes the polarization, and $\mathbf{\Upsilon}(\mathbf{r}, t)$ is the Gaussian white noise with zero mean and the correlation $\langle\Upsilon_\alpha(\mathbf{r}, t)\Upsilon_\beta(\mathbf{r}', t')\rangle = \delta_{\alpha,\beta}\delta(\mathbf{r} - \mathbf{r}')\delta(t - t')$ with $\alpha, \beta = x, y$. The coefficient χ is the "compressibility." From Eq. (6), it is straightforward to calculate the equal time correlation functions in Fourier space. The longitudinal velocity correlation function $\omega_\parallel(q)$ and static structure factor $S(q)$ are calculated as

$$\omega_\parallel(q) = \frac{\omega_0}{1 + (\xi_\parallel q)^2} \tag{7}$$

and

$$S(q) = \frac{S_0}{1 + (\xi_\parallel q)^2}, \tag{8}$$

respectively (see Appendix G). Here the values at $q = 0$ are given by $\omega_0 = v_0^2\tau_p/[2(\tau_m + \tau_p)]$ and $S_0 = \rho\zeta\chi v_0^2/2D$. $\xi_\parallel = \sqrt{\tau_p/[\rho\zeta\chi(1 + \tau_m/\tau_p)]}$ is the correlation length. The theory predicts that $\omega_\parallel(q)$ and $S(q)$ are characterized by the same correlation length $\xi_\parallel$, which supports numerical results shown in Figs. 3(a) and 3(d). Furthermore, Eq. (8) means that the density correlation function behaves as $S(q) \sim q^{-2}$ on length scales smaller than $\xi_\parallel$. From the argument above Eq. (5), this

yields GNF; $\Delta N \sim \langle N \rangle^1$ with the exponent $\alpha = 1$. The argument given above elucidates how GNF in our system arise due to the growth of the spatial longitudinal velocity correlation caused by persistence motion, and they are confined in the region of size $\xi_\parallel$. This also explains the numerical results in Fig. 4 qualitatively. We note that the linearized hydrodynamic theory can explain the growth of the correlations of the density and longitudinal velocity, but it cannot predict the growth of the transverse velocity or the vortex, as pointed out in Ref. [38].

Finally, we remark that the prediction of the linear hydrodynamic theory is only qualitative. Recall that the static structure factor $S(q)$ satisfies the scaling relation Eq. (5) with the exponent $\beta = 4\alpha - 2$ and β varies with Pe (cf. the inset of Fig. 4). In contrast, the linearized theory predicts the Ornstein-Zernike form with the fixed $\beta (= 2)$. Also, $S(q)$ obtained numerically is larger than predicted by the linearized theory at small wave numbers (see Appendix G). These observations suggest that nonlinear coupling of the fluctuations between different hydrodynamic modes is at play. Furthermore, as shown by the blue dashed line in Fig. 3(c), the fit by theoretical prediction of $\xi_\parallel$ [below Eq. (G42)] deviates from the numerical data. Note that, in the small M limit, our theoretical prediction for $\xi_\parallel$ is reduced to $\xi_\parallel \propto$ Pe$^{1/2}$ obtained theoretically for overdamped ABP [38]. Somehow the fit by $\xi_\parallel \propto$ Pe$^{1/2}$ [dotted line in Fig. 3(c)] works better than our theoretical prediction. More quantitative assessments of these results are left for feature work.

V. SUMMARY

In this paper, we studied the growing density or number fluctuations in the disordered homogeneous phase of ABP for a wide range of Péclet numbers. It was possible by introducing the inertia to the original overdamped ABP model, which suppresses MIPS and generates the disordered homogeneous fluid. This system is ideal for studying the inherent nonequilibrium fluctuations unimpeded by MIPS. We first confirmed that the spatial velocity correlation has two distinct correlation lengths, $\xi_\parallel$ and $\xi_\perp$, corresponding to the longitudinal and transverse modes, even at a relatively low density. $\xi_\perp$ corresponds to the size of vortex patterns, which is reminiscent of active turbulence in the simple spherical active matter [39]. $\xi_\parallel$ is longer than $\xi_\perp$ and grows with the Péclet number. The growing longitudinal velocity correlation is related to the spatial correlation of the density fluctuation or the structure factor $S(q)$. We found that $S(q)$ grows at small wave numbers with Péclet numbers and has the same characteristic length as the longitudinal velocity correlation function. The large density fluctuations in the wave vector space is nothing but the large number fluctuations, or GNF, in the real space. We measured the number fluctuation ΔN in a sub-box of the size ℓ and showed that it grows as $\Delta N \sim \langle N \rangle^\alpha$ with the exponent $\alpha > 0.5$. The exponent α increases monotonically with Péclet number. The largest sub-box size below which we observe GNF agrees with $\xi_\parallel$. These facts yield a scaling relation for $S(q)$ characterized by $\xi_\parallel$ and α. Our results provide a coherent picture of the origin of GNF observed in ABP. We address that the origin of GNF here is similar but strictly different from GNF observed in ordered active fluids [42,63]. In the ordered

active fluids such as the Vicsek model, the active nematic [5,60], or the self-propelled rods [58], GNF are understood as the "infection" of Goldstone modes of the ordered phase to the density field [2,4,40,41]. In our model, however, the system is globally disordered, and there is no Goldstone mode. Instead, the large spatial velocity correlation yields GNF. We also showed that our results can be captured by a linearized hydrodynamic theory qualitatively but not quantitatively. A quantitatively valid theoretical treatment would require an analysis that fully considers nonlinear couplings of fluctuations. Our results suggest that the anomalously large density fluctuations should be universally and ubiquitously present in various active matter systems, even without explicit global orders and phase separation.

APPENDIX A: SYSTEM SIZE DEPENDENCE OF PHASE BEHAVIOR

In Fig. 1, we have shown the "phase diagram" in (M, Pe) space and the phase boundary between the MIPS and homogeneous phase. We have chosen a relatively large simulation size of $N = 4 \times 10^4$ because the phase boundary is sensitive to the system size. In Fig. 5, we show the phase diagram obtained from the smaller system $N = 1 \times 10^4$. The red-lined panels are configurations for the parameters in which the system undergoes MIPS at a larger system size of $N = 4 \times 10^4$, as
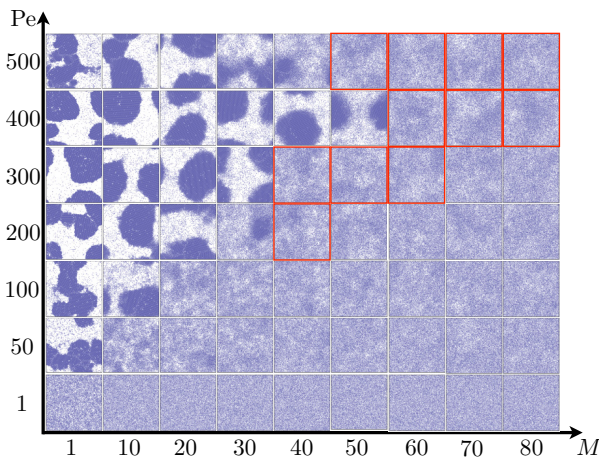

FIG. 5. The "phase diagram" of iABP for the system size $N = 1 \times 10^4$. Each panel is the snapshot of particle configuration for corresponding parameters (M, Pe). For the parameters indicated by the red-lined panels, the system undergoes MIPS for larger system size $N = 4 \times 10^4$.

shown in Fig. 1 of the main text. Furthermore, Fig. 5 shows that MIPS disappears at very large Pe ($\gtrsim 500$) in the small system. This re-entrant transition is reminiscent of the results shown by Mandal *et al.* [43], in which the inertia of both the position and the rotation (of the active noises) as well as the thermal noise are taken into account. We address that the re-entrance observed in our current model is the artifact due to the small system size.

APPENDIX B: CALCULATION OF COARSE-GRAINED DENSITY, VELOCITY, AND VORTICITY FIELDS

We have shown the coarse-grained density, velocity, and vorticity fields in Fig. 2 of the main text. These quantities are calculated as follows. The local density $\rho(\mathbf{r})$ is obtained by averaging the number of particles in a circle with a radius of 3σ placed on every node of a square-lattice with the lattice constant σ. The velocity field $\mathbf{v}(\mathbf{r})$ was obtained by taking the Gaussian-weighted average in a circle with a radius of 3σ. The value of the variance of the Gaussian function is chosen in such a way that the Gaussian function is 0.1 at $r = 3\sigma$. The vorticity field $\Omega(\mathbf{r}) = \partial_x v_y - \partial_y v_x$ is calculated as $\Omega(\mathbf{r}) \simeq \sum_{\text{cell}} \mathbf{v}(\mathbf{r}) \cdot \delta\mathbf{r}/\delta S_{\text{cell}}$, a line-integral along the circumference of a square cell with a side length 0.25σ. δS_{cell} is the area of the cell.

APPENDIX C: VELOCITY CORRELATION FUNCTION IN REAL SPACE

In Fig. 6(a), we show the velocity correlation function in real space [34,35], that is defined by

$$C(r) = \frac{1}{N}\left\langle \sum_{j \neq k} \mathbf{v}_j \cdot \mathbf{v}_k \delta(\mathbf{r} - \mathbf{r}_j + \mathbf{r}_k) \right\rangle. \quad (C1)$$

This is the Fourier transformation of $\omega(q) = \omega_\parallel(q) + \omega_\perp(q)$ introduced in the main text. One observes that the spatial velocity correlation grows as Pe increases in the real space. We fit the data by a function $C(r) = Ar^{-1/2}e^{-r/\lambda}$, which is the Fourier transformation of the Ornstein-Zernike function at large r [68]. The dashed lines in Fig. 6(b) are fits by this function. The fitting range is chosen as $r > 5$ for all Pe's. The triangle symbols in Fig. 6(b) represent the correlation length λ that is found by the fitting of $C(r)$. We find that $\lambda \simeq \xi_\perp$ and $C(r)$ is dominated by the transverse part. This is natural because $\xi_\perp \ll \xi_\parallel$ as seen in Fig. 6(b).

APPENDIX D: ENERGY SPECTRUM AND VELOCITY DISTRIBUTION

In the main text, we observed the development of the vortex structures whose spatial patterns are reminiscent of the turbulence. In the standard inertial turbulence of fluids at high Reynolds numbers, the fingerprint of the turbulence is the universal scale-free behavior of the energy spectrum, known as the Kolmogorov law [69]. A similar power law is also found in the energy spectrum in various active matter systems [7,8,46–54]. Such behaviors are aptly called active turbulence. However, the exponent of the power law depends on systems. Little is known about the universality of active turbulence. Here we show the energy spectrum of the iABP
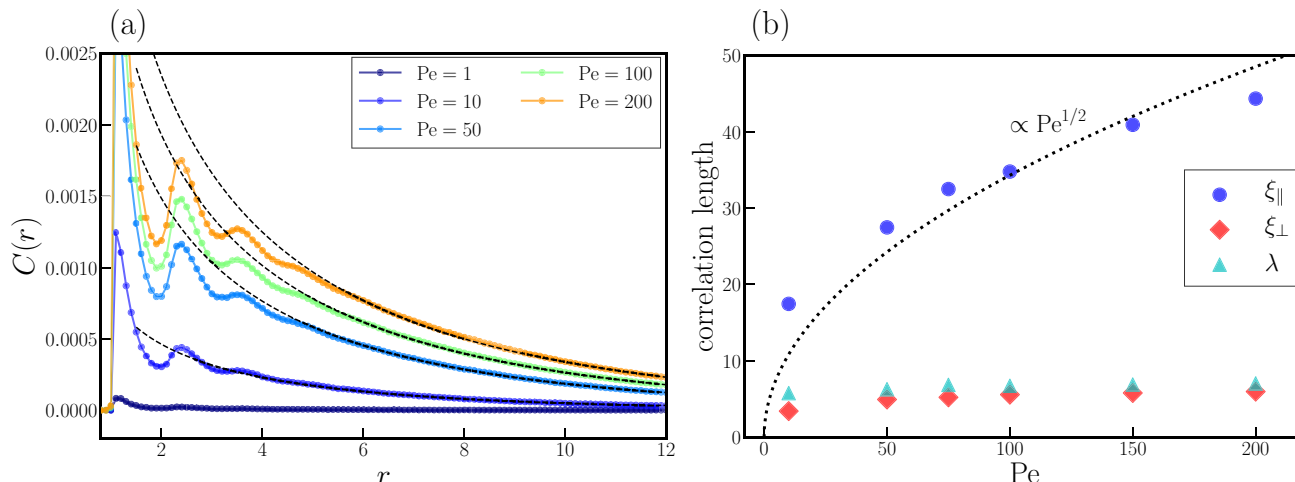
FIG. 6. (a) The velocity correlation function in the real space. The mass is fixed at $M = 80$. The dashed lines are fits by $C(r) = Ar^{-1/2}e^{-r/\lambda}$. (b) The correlation lengths of the velocity correlation function. The triangle symbols are the correlation length obtained from $C(r)$. The circles and diamonds are $\xi_\parallel$ and $\xi_\perp$ shown in Fig. 3(c) in the main text. The dotted line is a fit by $\xi_\parallel \propto Pe^{1/2}$.

model studied in the main text. In two dimensions, the energy spectrum is related to the velocity correlation function $\omega(q) = \omega_\parallel(q) + \omega_\perp(q)$ by

$$E(q) = 2\pi q \omega(q). \tag{D1}$$

In Fig. 7(a), the energy spectra $E(q)$ for several Pe's at $M = 80$ are shown. One observes a faint sign of the power law with the amplitudes increasing with Pe at intermediate wave numbers at $q \gtrsim 0.1$. A crude estimate of the exponent γ of the power law $E(q) \sim q^{-\gamma}$ is approximately equal to 0.6, which is much smaller than values reported in the past [7,8,46–54].

Recently, the non-Gaussianity of the velocity distribution has been reported in ABP and the active Ornstein-Uhlenbeck particles (AOUP) at high densities and high Pe [39,70]. We evaluated the velocity distribution to check if such deviation is also observed for low densities. In Fig. 7(b), we show the

velocity distribution for Pe = 1 and 200 at $M = 80$. The solid lines are the corresponding Gaussian distribution defined by

$$P(v) = \sqrt{\frac{M}{2\pi T_{\text{kin}}}} \exp\left(-\frac{Mv^2}{2T_{\text{kin}}}\right), \tag{D2}$$

where $T_{\text{kin}} = M\langle v_x^2 + v_y^2\rangle/2$ is the kinetic temperature. For both Pe's, the observed distribution functions are well fitted by the Gaussian, as in other systems at turbulent states [8,47,53].

APPENDIX E: DENSITY DEPENDENCE OF SPATIAL CORRELATIONS

In the main text, we showed spatial correlation functions only at $\rho = 0.5$. However, these large spatial correlations exist even at more low densities. Figure 8 represents spatial correlation functions for $\rho = 0.3$, 0.4, and 0.5. We confirm existence

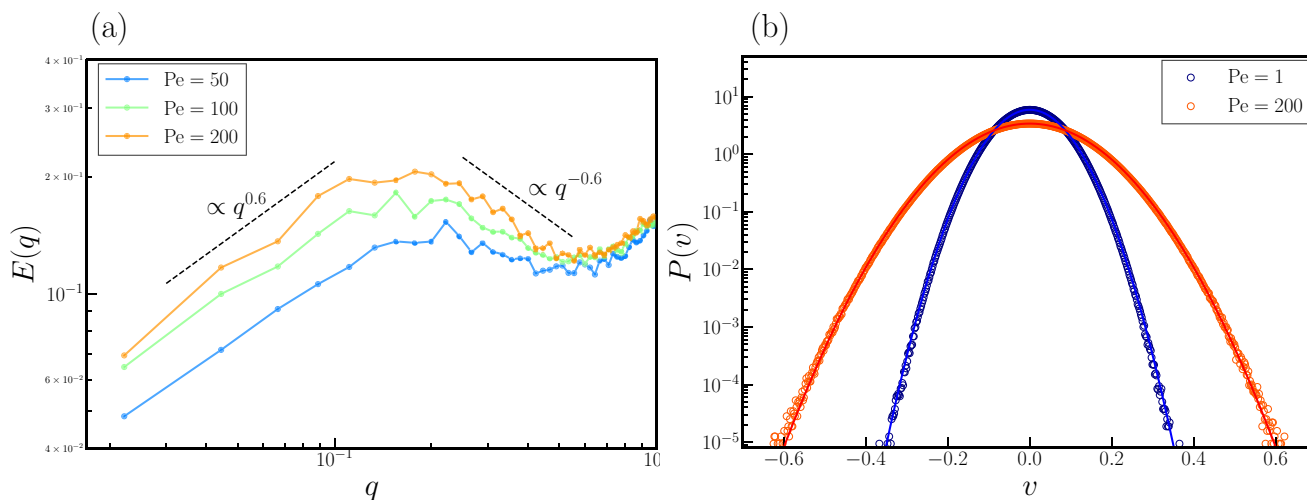FIG. 7. (a) The energy spectrum $E(q)$ for Pe = 50, 100, and 200 as a function of q. The mass is fixed at $M = 80$. The black broken lines of $q^{-0.6}$ and $q^{0.6}$ are guides for the eyes. (b) The velocity distribution function $P(v)$ for $M = 80$. The empty circles with blue and orange edge colors denote the numerical results for Pe = 1 and 200, respectively. The solid lines are fits by the Gaussian distribution.
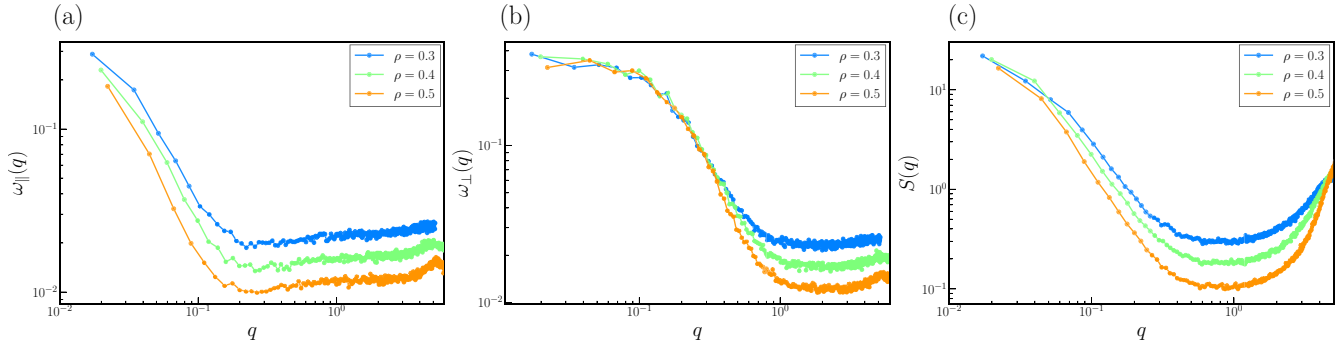
FIG. 8. Density dependence of spatial correlation functions at Pe = 200. The mass is fixed at $M = 80$. (a) The longitudinal velocity correlation function, (b) transverse velocity correlation function, and (c) static structure factor for $\rho = 0.3$, 0.4, and 0.5. All data are from the simulation with $N = 4 \times 10^4$.

of large correlations for all quantities, longitudinal velocity, transverse velocity, and density correlation functions. Hence, we conclude that the results in the main text are insensitive to the densities.

APPENDIX F: DENSITY CORRELATION IN MIPS PHASE

It is known that the system undergoing the phase separation with smooth surfaces develops the peak in the static structure factor characterized by a power law, $S(q) \propto q^{-(d+1)}$ in the low-wave-number regime. This is called Porod's law [55,56]. Porod's law is also observed in MIPS phase of active matter [22,26]. We show that Porod's law is also observed for iABP when the system undergoes MIPS. Figures 9(a)–9(c) are snapshots of the system undergoing MIPS for several M's. The colors represent the local density calculated by averaging the number of particles in a circle with a radius of 3σ. For the smallest inertia, $M = 1$, the phase boundary is sharp, and their surface is smooth. When $M = 30$ and 80, on the other hand, the phase boundaries become diffusive, and the surfaces are blurred. This behavior might be related to the difference in the (effective) temperatures between the dense and gas phase in the presence of inertia [43]. In Fig. 9(d), we show the static structure factor $S(q)$ for $M = 1$, 30, and 80. For $M = 1$, Porod's law, i.e., $S(q) \propto q^{-3}$, is clearly observed at low q's [22,26]. For the higher inertia, $M = 30$ and 80, $S(q)$ deviates from Porod's law, although the heights of $S(q)$ at low q's are unaltered. This behavior should be the consequence of the change in the sharpness of the phase boundaries.

In any case, we address that the development of the peak of $S(q)$ at low q's reported in the main text is distinct from trivial Porod's law of MIPS.

APPENDIX G: FLUCTUATING HYDRODYNAMIC DESCRIPTION

In Sec. IV of the main text, we employed an effective hydrodynamic description to elucidate the qualitative mechanism of the large density fluctuations or GNF. Here, we derive an effective hydrodynamic equation for iABP by following Dean's method [66,67], and calculate the longitudinal velocity correlation function and static structure factor.

1. Derivation of the fluctuating hydrodynamic equations

Our stating point is the equation of motion for the iABP in two dimensions:

$$\frac{d\boldsymbol{r}_j(t)}{dt} = \boldsymbol{v}_j(t), \tag{G1}$$

$$m\frac{d\boldsymbol{v}_j(t)}{dt} = -\zeta \boldsymbol{v}_j(t) - \sum_{k=1}^{N} \nabla_j U(r_{jk}) + \zeta v_0 \boldsymbol{e}[\phi_j(t)], \tag{G2}$$

$$\frac{d\phi_j(t)}{dt} = \sqrt{\frac{2}{\tau_p}}\eta_j(t). \tag{G3}$$

Here $\eta_j(t)$ is a white noise that satisfies $\langle \eta_j(t) \rangle = 0$ and $\langle \eta_j(t)\eta_k(t') \rangle = \delta_{j,k}\delta(t - t')$ and $U(r)$ is the pairwise potential. We assume that $\nabla U(0) = \boldsymbol{0}$ for simplicity. $\boldsymbol{e}(\phi) = (\cos\phi, \sin\phi)$ is the unit vector pointing to the direction of the active random force. Hydrodynamic fields of this system are the number density

$$\rho(\boldsymbol{r}, t) = \sum_{j=1}^{N} \delta[\boldsymbol{r} - \boldsymbol{r}_j(t)], \tag{G4}$$

density current

$$\boldsymbol{J}(\boldsymbol{r}, t) = \sum_{j=1}^{N} \boldsymbol{v}_j(t)\delta[\boldsymbol{r} - \boldsymbol{r}_j(t)], \tag{G5}$$

and polarization

$$\boldsymbol{p}(\boldsymbol{r}, t) = \sum_{j=1}^{N} \boldsymbol{e}[\phi_j(t)]\delta[\boldsymbol{r} - \boldsymbol{r}_j(t)]. \tag{G6}$$

By differentiating these hydrodynamic fields with respect to time, we obtain the following set of equations. For the density, it is the continuum equation;

$$\partial_t \rho(\boldsymbol{r}, t) = -\nabla \cdot \boldsymbol{J}(\boldsymbol{r}, t). \tag{G7}$$

For the current and the polarization fields,

$$m\partial_t \boldsymbol{J}(\boldsymbol{r}, t) = -\nabla \cdot \mathsf{M}^{vv}(\boldsymbol{r}, t) - \zeta \boldsymbol{J}(\boldsymbol{r}, t)$$

$$- \rho(\boldsymbol{r}, t)\sum_{k=1}^{N} \nabla U(\boldsymbol{r} - \boldsymbol{r}_k) + \zeta v_0 \boldsymbol{p}(\boldsymbol{r}, t), \tag{G8}$$
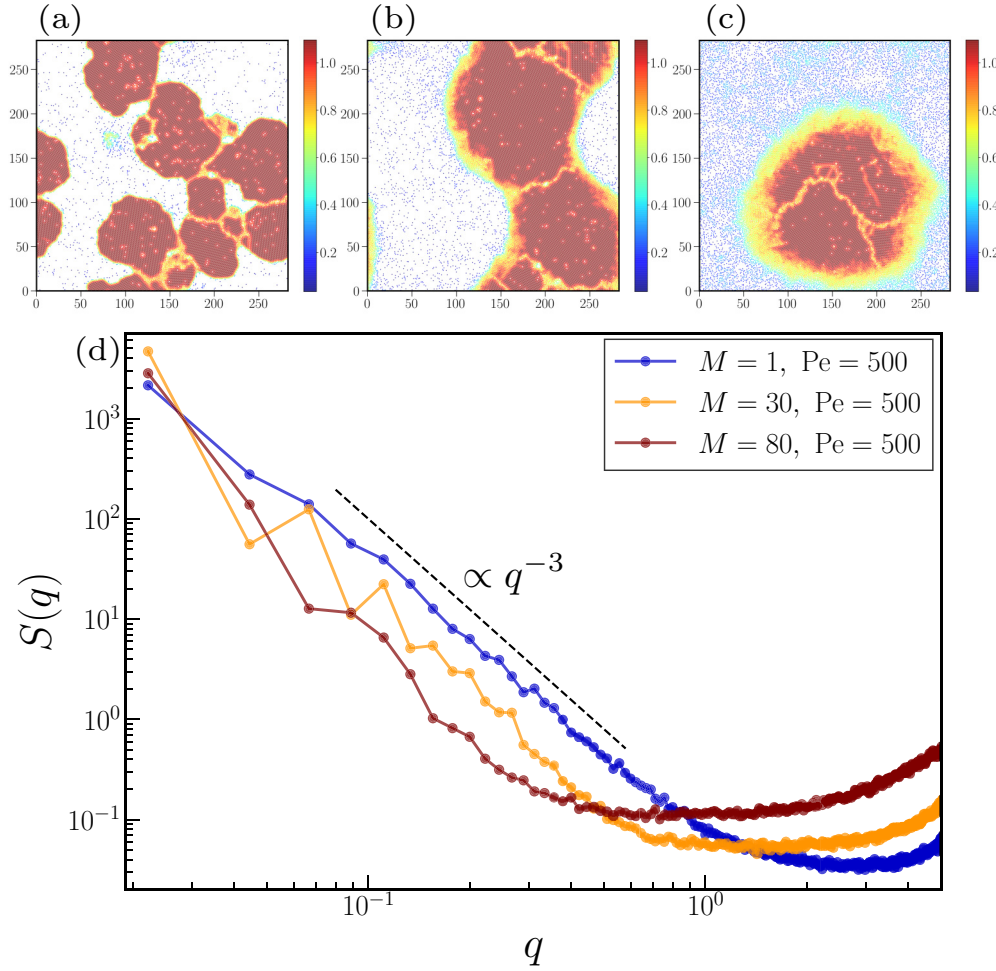
FIG. 9. Snapshots in MIPS phases for Pe = 500, (a) $M = 1$, (b) $M = 30$, and (c) $M = 80$. The color bar indicates the magnitude of density. The system size is $N = 4 \times 10^4$. (d) The static structure factor $S(q)$ for each parameter.

$$\partial_t \boldsymbol{p}(\boldsymbol{r}, t) = -\nabla \cdot [\mathsf{M}^{\mathrm{ev}}(\boldsymbol{r}, t)]^T - \sum_{j=1}^{N} \frac{d\boldsymbol{e}[\phi_j(t)]}{dt} \delta[\boldsymbol{r} - \boldsymbol{r}_j(t)],$$

$$\text{(G9)}$$

where tensors $\mathsf{M}^{\mathrm{vv}}(\boldsymbol{r}, t)$ and $\mathsf{M}^{\mathrm{ev}}(\boldsymbol{r}, t)$ are defined by

$$\mathsf{M}^{\mathrm{vv}}(\boldsymbol{r}, t) := m \sum_{j=1}^{N} \boldsymbol{v}_j(t) \boldsymbol{v}_j(t) \delta[\boldsymbol{r} - \boldsymbol{r}_j(t)], \qquad \text{(G10)}$$

$$\mathsf{M}^{\mathrm{ev}}(\boldsymbol{r}, t) := \sum_{j=1}^{N} \boldsymbol{e}[\phi_j(t)] \boldsymbol{v}_j(t) \delta[\boldsymbol{r} - \boldsymbol{r}_j(t)]. \qquad \text{(G11)}$$

These tensors can be rewritten in terms of hydrodynamic fields, following the procedure discussed in Ref. [67], as

$$\mathsf{M}^{\mathrm{vv}}(\boldsymbol{r}, t) = \frac{m \boldsymbol{J}(\boldsymbol{r}, t) \boldsymbol{J}(\boldsymbol{r}, t)}{\rho(\boldsymbol{r}, t)}, \qquad \text{(G12)}$$

$$\mathsf{M}^{\mathrm{ev}}(\boldsymbol{r}, t) = \frac{\boldsymbol{p}(\boldsymbol{r}, t) \boldsymbol{J}(\boldsymbol{r}, t)}{\rho(\boldsymbol{r}, t)}. \qquad \text{(G13)}$$

The potential part in the right-hand side of Eq. (G8) can be expressed as

$$\sum_{k=1}^{N} \nabla U(|\boldsymbol{r} - \boldsymbol{r}_k|) = \nabla \frac{\delta \mathcal{F}[\rho(\cdot, t)]}{\delta \rho(\boldsymbol{r}, t)}, \qquad \text{(G14)}$$

where the functional $\mathcal{F}[\rho]$ is defined by

$$\mathcal{F}[\rho(\cdot, t)] := \frac{1}{2} \int_V d^2\boldsymbol{r} \int_V d^2\boldsymbol{r}' \, \rho(\boldsymbol{r}, t) \rho(\boldsymbol{r}', t) U(|\boldsymbol{r} - \boldsymbol{r}'|).$$

$$\text{(G15)}$$

Substituting these expressions, Eq. (G8) becomes

$$m \partial_t \boldsymbol{J}(\boldsymbol{r}, t) = -\nabla \cdot \left[\frac{m \boldsymbol{J}(\boldsymbol{r}, t) \boldsymbol{J}(\boldsymbol{r}, t)}{\rho(\boldsymbol{r}, t)} \right] - \zeta \boldsymbol{J}(\boldsymbol{r}, t)$$
$$- \rho(\boldsymbol{r}, t) \nabla \frac{\delta \mathcal{F}[\rho(\cdot, t)]}{\delta \rho(\boldsymbol{r}, t)} + \zeta v_0 \boldsymbol{p}(\boldsymbol{r}, t). \quad \text{(G16)}$$

Next, we derive the equation for polarization. The time derivative of the unit vector $\boldsymbol{e}[\phi_j(t)]$ in right-hand side of

Eq. (G9) is given by

$$\frac{d\boldsymbol{e}[\phi_j(t)]}{dt} = \sqrt{\frac{2}{\tau_p}} \begin{bmatrix} -\sin\phi_j(t) \\ \cos\phi_j(t) \end{bmatrix} \circ \eta_j(t)$$

$$= -\frac{1}{\tau_p}\boldsymbol{e}_j(t) + \sqrt{\frac{2}{\tau_p}} \begin{bmatrix} -\sin\phi_j(t) \\ \cos\phi_j(t) \end{bmatrix} \bullet \eta_j(t), \quad \text{(G17)}$$

where the symbols $\circ$ and $\bullet$ denote the Stratonovich and Itô product, respectively. We have adopted the Itô representation for the multiplicative noise to ensure that the average of the noise is zero [71]. Using Eq. (G17), Eq. (G9) is rewritten as

$$\partial_t \boldsymbol{p}(\boldsymbol{r},t) = -\frac{1}{\tau_p}\boldsymbol{p}(\boldsymbol{r},t) - \nabla \cdot \left[\frac{\boldsymbol{J}(\boldsymbol{r},t)\boldsymbol{p}(\boldsymbol{r},t)}{\rho(\boldsymbol{r},t)}\right] + \boldsymbol{\Lambda}(\boldsymbol{r},t),$$
$$\text{(G18)}$$

where the noise term $\boldsymbol{\Lambda}(\boldsymbol{r},t)$ is defined as

$$\boldsymbol{\Lambda}(\boldsymbol{r},t) := \sqrt{\frac{2}{\tau_p}} \sum_{j=1}^{N} \begin{bmatrix} -\sin\phi_j(t) \\ \cos\phi_j(t) \end{bmatrix} \bullet \eta_j(t)\delta[\boldsymbol{r} - \boldsymbol{r}_j(t)].$$
$$\text{(G19)}$$

We rewrite this noise as

$$\boldsymbol{\Lambda}(\boldsymbol{r},t) = \sqrt{\frac{\rho(\boldsymbol{r},t)}{\tau_p}}\boldsymbol{\Upsilon}(\boldsymbol{r},t), \quad \text{(G20)}$$

which satisfies $\langle \Upsilon_\alpha(\boldsymbol{r},t)\rangle = 0$ and

$$\langle \Upsilon_\alpha(\boldsymbol{r},t)\Upsilon_\beta(\boldsymbol{r}',t')\rangle = \delta_{\alpha,\beta}\delta(\boldsymbol{r}-\boldsymbol{r}')\delta(t-t'). \quad \text{(G21)}$$

We can prove Eq. (G21), by calculating the each component of noise correlations and compare the results from Eq. (G19). For example, the (x,x) component is calculated as

$$\langle \Lambda_x(\boldsymbol{r},t)\Lambda_x(\boldsymbol{r}',t')\rangle = \frac{2}{\tau_p}\sum_{j=1}^{N}\langle \sin^2\phi_j(t)\rangle\delta[\boldsymbol{r}-\boldsymbol{r}_j(t)]$$

$$\times \delta(\boldsymbol{r}-\boldsymbol{r}')\delta(t-t'). \quad \text{(G22)}$$

Using Eq. (G3), the expectation value of $\sin^2\phi_j(t)$ can be obtained as

$$\langle \sin^2\phi_j(t)\rangle = \tfrac{1}{2} - \tfrac{1}{2}\cos[2\phi_j(0)]e^{-4t/\tau_p}. \quad \text{(G23)}$$

The summation $\sum_{j=1}^{N}\cos[2\phi_j(0)]$ becomes 0 in the limits of $N \to \infty$ because the initial value of angles $\phi_j(0)$ is completely random. Hence, in the limit of $N \to \infty$, Eq. (G22) becomes

$$\langle \Lambda_x(\boldsymbol{r},t)\Lambda_x(\boldsymbol{r}',t')\rangle = \frac{\rho(\boldsymbol{r},t)}{\tau_p}\delta(\boldsymbol{r}-\boldsymbol{r}')\delta(t-t'). \quad \text{(G24)}$$

The (y,y) component of Eq. (G19) is also given by Eq. (G24) in the limit of $N \to \infty$. The correlation function between x and y component of Eq. (G19) becomes 0 by using the relation

$$\langle \sin\phi_j(t)\cos\phi_j(t)\rangle = \tfrac{1}{2}\sin[2\phi_j(0)]e^{-4t/\tau_p}. \quad \text{(G25)}$$

It is noteworthy that the noise correlation for the polarization field is identical to those of another, or simpler, active matter model known as the AOUP model [72], in the continuum limit.

Below, we summarize the derived fluctuating hydrodynamic equation for iABP;

$$\partial_t \rho(\boldsymbol{r},t) = -\nabla \cdot \boldsymbol{J}(\boldsymbol{r},t), \quad \text{(G26)}$$

$$m\partial_t \boldsymbol{J}(\boldsymbol{r},t) = -\nabla \cdot \mathsf{P}(\boldsymbol{r},t) - \zeta \boldsymbol{J}(\boldsymbol{r},t)$$

$$-\nabla \cdot \left[\frac{m\boldsymbol{J}(\boldsymbol{r},t)\boldsymbol{J}(\boldsymbol{r},t)}{\rho(\boldsymbol{r},t)}\right] + \zeta v_0\boldsymbol{p}(\boldsymbol{r},t), \quad \text{(G27)}$$

$$\partial_t \boldsymbol{p}(\boldsymbol{r},t) = -\frac{1}{\tau_p}\boldsymbol{p}(\boldsymbol{r},t) - \nabla \cdot \left[\frac{\boldsymbol{J}(\boldsymbol{r},t)\boldsymbol{p}(\boldsymbol{r},t)}{\rho(\boldsymbol{r},t)}\right]$$

$$+ \sqrt{\frac{\rho(\boldsymbol{r},t)}{\tau_p}}\boldsymbol{\Upsilon}(\boldsymbol{r},t), \quad \text{(G28)}$$

with the pressure tensor $\mathsf{P}(\boldsymbol{r},t)$ defined by

$$\nabla \cdot \mathsf{P}(\boldsymbol{r},t) := \rho(\boldsymbol{r},t)\nabla\frac{\delta\mathcal{F}[\rho(\cdot,t)]}{\delta\rho(\boldsymbol{r},t)}. \quad \text{(G29)}$$

Now let us consider the linearization of the fluctuating hydrodynamics of iABP so that we can derive the correlation functions. We assume that the pressure tensor Eq. (G29) depends only on the density field. To the linear order in the density fluctuation $\delta\rho(\boldsymbol{r},t) = \rho(\boldsymbol{r},t) - \rho$ in the hydrodynamic limit [38], we have

$$\nabla \cdot \mathsf{P}(\boldsymbol{r},t) \simeq \frac{1}{\rho\chi}\nabla\delta\rho(\boldsymbol{r},t). \quad \text{(G30)}$$

Here χ is a "compressibility" defined by $\chi^{-1} := \rho\partial P/\partial\rho|_{\rho(\boldsymbol{r})=\rho}$ where P is a diagonal component of $\mathsf{P}(\boldsymbol{r},t)$. Linearizing Eqs. (G26)–(G28) and using Eq. (G30), we arrive at

$$\partial_t \delta\rho(\boldsymbol{r},t) = -\nabla \cdot \delta\boldsymbol{J}(\boldsymbol{r},t), \quad \text{(G31)}$$

$$m\partial_t \delta\boldsymbol{J}(\boldsymbol{r},t) = -\frac{1}{\rho\chi}\nabla\delta\rho(\boldsymbol{r},t) - \zeta\delta\boldsymbol{J}(\boldsymbol{r},t) + \zeta v_0\delta\boldsymbol{p}(\boldsymbol{r},t),$$
$$\text{(G32)}$$

$$\partial_t \delta\boldsymbol{p}(\boldsymbol{r},t) = -\frac{1}{\tau_p}\delta\boldsymbol{p}(\boldsymbol{r},t) + \sqrt{\frac{\rho}{\tau_p}}\boldsymbol{\Upsilon}(\boldsymbol{r},t). \quad \text{(G33)}$$

Note that the equation for the polarization fluctuation Eq. (G33) is a simple Ornstein-Uhlenbeck process and, thus, we can regard $\delta\boldsymbol{p}(\boldsymbol{r},t)$ as a colored noise of Eq. (G32). In other words, Eq. (G32) is written as

$$m\partial_t \delta\boldsymbol{J}(\boldsymbol{r},t) = -\frac{1}{\rho\chi}\nabla\delta\rho(\boldsymbol{r},t) - \zeta\delta\boldsymbol{J}(\boldsymbol{r},t) + \boldsymbol{\Xi}^{\mathrm{act}}(\boldsymbol{r},t),$$
$$\text{(G34)}$$

with an active noise $\boldsymbol{\Xi}^{\mathrm{act}}(\boldsymbol{r},t) := \zeta v_0\delta\boldsymbol{p}(\boldsymbol{r},t)$ whose correlation is written as

$$\langle \Xi_\alpha^{\mathrm{act}}(\boldsymbol{r},t)\Xi_\beta^{\mathrm{act}}(\boldsymbol{r}',t')\rangle = \frac{v_0^2\zeta^2\rho}{2}e^{-|t-t'|/\tau_p}\delta_{\alpha,\beta}\delta(\boldsymbol{r}-\boldsymbol{r}').$$
$$\text{(G35)}$$

In the limit of $\tau_p \to 0$, the active noise becomes white noise and the fluctuation dissipation relation is recovered.
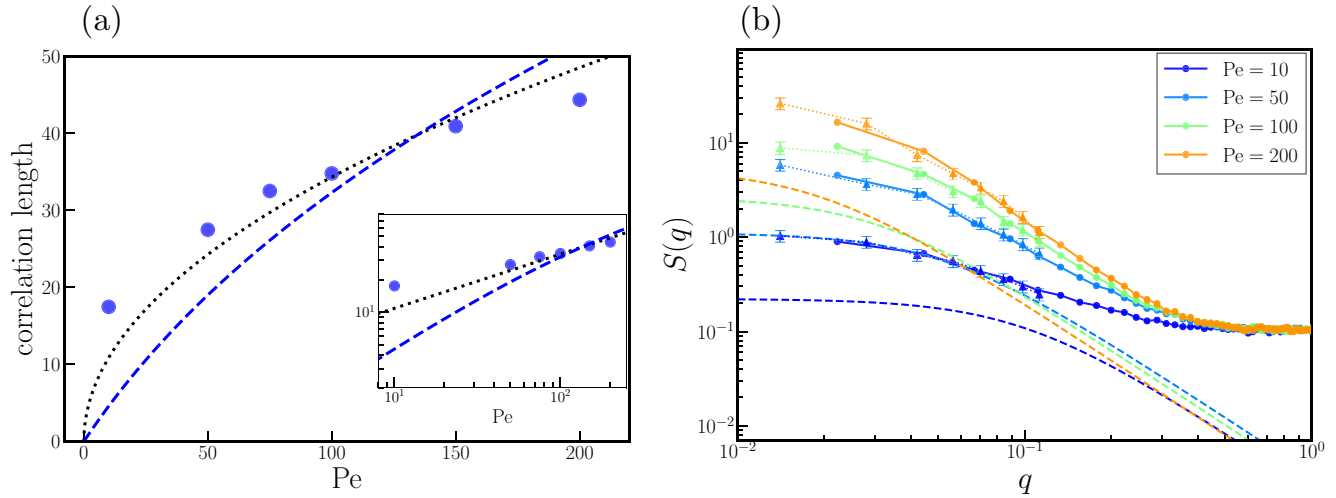
FIG. 10. (a) Numerical data and the fit by the theory [second equation of Eq. (G40)] of the longitudinal correlation length $\xi_\parallel$ [identical to Fig. 3(c) in the main text]. The inset is the log-log plot of the same data. The blue dots represent the numerical values. The blue dashed line is the fitting curve of the second equation of Eq. (G40). The fitting parameter are found to be $b\tau_v/\sigma^2 \simeq 18.8$. The black dotted line represents the prediction from the overdamped ABP, $\xi_\parallel \propto \text{Pe}^{1/2}$. Panel (b) is the numerical results of the static structure factor. Dashed lines represent the theoretical prediction of Eq. (G42) drawn by using the fitting parameter obtained from panel (a).

Recently, Marconi *et al.* [45] has derived similar fluctuating hydrodynamic equations for the underdamped ABP and AOUP model starting from the BBGKY hierarchy.

2. Velocity and density correlation functions

From Eqs. (G31) and (G34), we can easily calculate the longitudinal velocity and density correlation function. By Fourier transforming in time and space, Eq. (G31) and (G34) are written as

$$-i\omega\delta\check{\rho}(\boldsymbol{q}, \omega) = -iq\delta\check{J}_\parallel(\boldsymbol{q}, \omega), \tag{G36}$$

$$-i\omega\delta\check{J}_\parallel(\boldsymbol{q}, \omega) = -i\gamma bq\delta\check{\rho}(\boldsymbol{q}, \omega) - \gamma\delta\check{J}_\parallel(\boldsymbol{q}, \omega) + \frac{1}{m}\check{\Xi}_x^{\text{act}}(\boldsymbol{q}, \omega), \tag{G37}$$

where $\gamma = \zeta/m$ and $b = 1/(\rho\zeta\chi)$. The variables with check symbol $\check{X}(\boldsymbol{q}, \omega)$ represent the Fourier transformed quantities with respect to $\boldsymbol{r}$ and t. By eliminating the density field from Eq. (G37) and using the Wiener-Khinchin theorem, we obtain the dynamical longitudinal velocity correlation function in Fourier space:

$$
\begin{aligned}
\omega_\parallel(q, \omega) &= \frac{1}{N}\int_{-\infty}^\infty dt \, \langle\delta\tilde{J}_\parallel(\boldsymbol{q}, t)\delta\tilde{J}_\parallel^*(\boldsymbol{q}, 0)\rangle e^{i\omega t} \\
&= \frac{v_0^2\gamma^2 D\omega^2}{[(\omega^2 - \gamma bq^2)^2 + \gamma^2\omega^2](\omega^2 + D^2)},
\end{aligned} \tag{G38}
$$

where $D = 1/\tau_p$ and the variables with tildes, $\tilde{X}(\boldsymbol{q}, t)$, are the Fourier transformed variables with respect to $\boldsymbol{r}$. By integrating Eq. (G38) over ω, we obtain the equal time correlation function,

$$\omega_\parallel(q) = \frac{1}{2\pi}\int_{-\infty}^\infty d\omega \, \omega_\parallel(q, \omega) = \frac{\omega_0}{1 + (\xi_\parallel q)^2}, \tag{G39}$$

with

$$
\begin{aligned}
\omega_0 &:= \frac{v_0^2\gamma}{2(D + \gamma)} = \frac{v_0^2\tau_p}{2(\tau_m + \tau_p)}, \\
\xi_\parallel^2 &:= \frac{b\gamma}{D(D + \gamma)} = \frac{b\tau_p}{1 + \tau_m/\tau_p}.
\end{aligned} \tag{G40}
$$

Here $\tau_m = 1/\gamma$ is the inertial relaxation time. Next, we calculate the density correlation function. Using Eq. (G36), the dynamical structure factor is written as

$$
\begin{aligned}
S(q, \omega) &= \frac{q^2}{\omega^2}\omega_\parallel(q, \omega) \\
&= \frac{v_0^2\gamma^2 Dq^2}{[(\omega^2 - \gamma bq^2)^2 + \gamma^2\omega^2](\omega^2 + D^2)}.
\end{aligned} \tag{G41}
$$

By integrating over ω, we obtain the static structure factor given by

$$S(q) = \frac{1}{2\pi}\int_{-\infty}^\infty d\omega \, S(q, \omega) = \frac{S_0}{1 + (\xi_\parallel q)^2} \tag{G42}$$

with

$$S_0 := \frac{v_0^2}{2bD} = \frac{1}{2}v_0^2\tau_p\zeta\rho\chi = \rho T_{\text{eff}}\chi, \tag{G43}$$

where we defined the effective temperature by $T_{\text{eff}} := v_0^2\tau_p\zeta/2$. Both $\omega_\parallel(q)$ and $S(q)$ are of the Ornstein-Zernike type are characterized by a single correlation length $\xi_\parallel$.

3. Comparison of the linearized theory with numerical results

Here we quantitatively compare simulation results to theoretical prediction. The filled circles in Fig. 10(a) are the same data for $\xi_\parallel$ presented in Fig. 3(c) in the main text. Recall that $\xi_\parallel$'s are obtained by fitting $\omega_\parallel(q)$ with the Ornstein-Zernike function. We fit the data by our theoretical prediction, the

second equation of Eq. (G40), (dashed lines) using $b\tau_v/\sigma^2 = 18.8$ as a fitting parameter. The dotted line is $\xi_\parallel \propto \sqrt{\text{Pe}}$ which was predicted by the overdamped ABP in Refs. [37,38] and works better than our theoretical prediction. However, since the differences between the two predictions are not large, it is early to decide which scaling works better. Using the fitting parameter obtained from Fig. 10(a), we compare

the simulated $S(q)$ with theoretical prediction, Eq. (G42). Substantial discrepancies between simulation data and theoretical prediction can not be remedied by a slight change of the fitting parameter $b\tau_v/\sigma^2$ and, therefore, implies that the nonlinear coupling of the fluctuations, which are completely absent in our theoretical analysis, is not negligible at large Pe's.

[1] C. Bechinger, R. Di Leonardo, H. Löwen, C. Reichhardt, G. Volpe, and G. Volpe, Active particles in complex and crowded environments, Rev. Mod. Phys. **88**, 045006 (2016).

[2] M. C. Marchetti, J. F. Joanny, S. Ramaswamy, T. B. Liverpool, J. Prost, M. Rao, and R. A. Simha, Hydrodynamics of soft active matter, Rev. Mod. Phys. **85**, 1143 (2013).

[3] S. Ramaswamy, The mechanics and statistics of active matter, Annu. Rev. Condens. Matter Phys. **1**, 323 (2010).

[4] S. Ramaswamy, R. A. Simha, and J. Toner, Active nematics on a substrate: Giant number fluctuations and long-time tails, Europhys. Lett. **62**, 196 (2003).

[5] H. Chaté, F. Ginelli, and R. Montagne, Simple Model for Active Nematics: Quasi-long-range Order and Giant Fluctuations, Phys. Rev. Lett. **96**, 180602 (2006).

[6] V. Narayan, S. Ramaswamy, and N. Menon, Long-lived giant number fluctuations in a swarming granular nematic, Science **317**, 105 (2007).

[7] C. Dombrowski, L. Cisneros, S. Chatkaew, R. E. Goldstein, and J. O. Kessler, Self-concentration and Large-scale Coherence in Bacterial Dynamics, Phys. Rev. Lett. **93**, 098103 (2004).

[8] H. H. Wensink, J. Dunkel, S. Heidenreich, K. Drescher, R. E. Goldstein, H. Löwen, and J. M. Yeomans, Meso-scale turbulence in living fluids, Proc. Natl. Acad. Sci. USA **109**, 14308 (2012).

[9] J. Tailleur and M. E. Cates, Statistical Mechanics of Interacting Run-and-Tumble Bacteria, Phys. Rev. Lett. **100**, 218103 (2008).

[10] Y. Fily and M. C. Marchetti, Athermal Phase Separation of Self-propelled Particles with no Alignment, Phys. Rev. Lett. **108**, 235702 (2012).

[11] J. Stenhammar, A. Tiribocchi, R. J. Allen, D. Marenduzzo, and M. E. Cates, Continuum Theory of Phase Separation Kinetics for Active Brownian Particles, Phys. Rev. Lett. **111**, 145702 (2013).

[12] J. Bialké, H. Löwen, and T. Speck, Microscopic theory for the phase separation of self-propelled repulsive disks, Europhys. Lett. **103**, 30008 (2013).

[13] T. Speck, J. Bialké, A. M. Menzel, and H. Löwen, Effective Cahn-Hilliard Equation for the Phase Separation of Active Brownian Particles, Phys. Rev. Lett. **112**, 218304 (2014).

[14] T. Speck, A. M. Menzel, J. Bialké, and H. Löwen, Dynamical mean-field theory and weakly non-linear analysis for the phase separation of active brownian particles, J. Chem. Phys. **142**, 224109 (2015).

[15] R. Wittkowski, A. Tiribocchi, J. Stenhammar, R. J. Allen, D. Marenduzzo, and M. E. Cates, Scalar φ^4 field theory for active-particle phase separation, Nat. Commun. **5**, 4351 (2014).

[16] M. E. Cates and J. Tailleur, Motility-induced phase separation, Annu. Rev. Condens. Matter Phys. **6**, 219 (2015).

[17] G. S. Redner, C. G. Wagner, A. Baskaran, and M. F. Hagan, Classical Nucleation Theory Description of Active Colloid Assembly, Phys. Rev. Lett. **117**, 148002 (2016).

[18] A. P. Solon, J. Stenhammar, M. E. Cates, Y. Kafri, and J. Tailleur, Generalized thermodynamics of phase equilibria in scalar active matter, Phys. Rev. E **97**, 020602(R) (2018).

[19] T. Arnoulx de Pirey, G. Lozano, and F. van Wijland, Active Hard Spheres in Infinitely Many Dimensions, Phys. Rev. Lett. **123**, 260602 (2019).

[20] G. S. Redner, M. F. Hagan, and A. Baskaran, Structure and Dynamics of a Phase-separating Active Colloidal Fluid, Phys. Rev. Lett. **110**, 055701 (2013).

[21] Y. Fily, S. Henkes, and M. C. Marchetti, Freezing and phase separation of self-propelled disks, Soft Matter **10**, 2132 (2014).

[22] J. Stenhammar, D. Marenduzzo, R. J. Allen, and M. E. Cates, Phase behaviour of active Brownian particles: The role of dimensionality, Soft Matter **10**, 1489 (2014).

[23] D. Levis, J. Codina, and I. Pagonabarraga, Active brownian equation of state: Metastability and phase coexistence, Soft Matter **13**, 8113 (2017).

[24] J. T. Siebert, F. Dittrich, F. Schmid, K. Binder, T. Speck, and P. Virnau, Critical behavior of active Brownian particles, Phys. Rev. E **98**, 030601(R) (2018).

[25] P. Digregorio, D. Levis, A. Suma, L. F. Cugliandolo, G. Gonnella, and I. Pagonabarraga, Full Phase Diagram of Active Brownian Disks: From Melting to Motility-induced Phase Separation, Phys. Rev. Lett. **121**, 098003 (2018).

[26] C. B. Caporusso, P. Digregorio, D. Levis, L. F. Cugliandolo, and G. Gonnella, Motility-induced Microphase and Macrophase Separation in a Two-dimensional Active Brownian Particle System, Phys. Rev. Lett. **125**, 178004 (2020).

[27] T. F. F. Farage, P. Krinninger, and J. M. Brader, Effective interactions in active Brownian suspensions, Phys. Rev. E **91**, 042310 (2015).

[28] A. P. Solon, J. Stenhammar, M. E. Cates, Y. Kafri, and J. Tailleur, Generalized thermodynamics of motility-induced phase separation: Phase equilibria, laplace pressure, and change of ensembles, New J. Phys. **20**, 075001 (2018).

[29] T. Speck, Coexistence of active Brownian disks: van der waals theory and analytical results, Phys. Rev. E **103**, 012607 (2021).

[30] J. Bialké, J. T. Siebert, H. Löwen, and T. Speck, Negative Interfacial Tension in Phase-separated Active Brownian Particles, Phys. Rev. Lett. **115**, 098301 (2015).

[31] E. Tjhung, C. Nardini, and M. E. Cates, Cluster Phases and Bubbly Phase Separation in Active Fluids: Reversal of the Ostwald Process, Phys. Rev. X **8**, 031080 (2018).

[32] X.-q. Shi, G. Fausti, H. Chaté, C. Nardini, and A. Solon, Self-organized Critical Coexistence Phase in Repulsive Active Particles, Phys. Rev. Lett. **125**, 168001 (2020).

[33] L. Caprini, U. Marini Bettolo Marconi, and A. Puglisi, Spontaneous Velocity Alignment in Motility-induced Phase Separation, Phys. Rev. Lett. **124**, 078001 (2020).

[34] L. Caprini, Umberto Marini Bettolo Marconi, C. Maggi, M. Paoluzzi, and A. Puglisi, Hidden velocity ordering in dense suspensions of self-propelled disks, Phys. Rev. Res. **2**, 023321 (2020).

[35] L. Caprini and U. Marini Bettolo Marconi, Spatial velocity correlations in inertial systems of active Brownian particles, Soft Matter **17**, 4109 (2021).

[36] E. Flenner, G. Szamel, and L. Berthier, The nonequilibrium glassy dynamics of self-propelled particles, Soft Matter **12**, 7136 (2016).

[37] S. Henkes, K. Kostanjevec, J. M. Collinson, R. Sknepnek, and E. Bertin, Dense active matter model of motion patterns in confluent cell monolayers, Nat. Commun. **11**, 1405 (2020).

[38] G. Szamel and E. Flenner, Long-ranged velocity correlations in dense systems of self-propelled particles, Europhys. Lett. **133**, 60002 (2021).

[39] Y.-E. Keta, R. L. Jack, and L. Berthier, Disordered Collective Motion in Dense Assemblies of Persistent Particles, Phys. Rev. Lett. **129**, 048002 (2022).

[40] J. Toner and Y. Tu, Long-range Order in a Two-dimensional Dynamical XY Model: How Birds Fly Together, Phys. Rev. Lett. **75**, 4326 (1995).

[41] J. Toner, Y. Tu, and S. Ramaswamy, Hydrodynamics and phases of flocks, Ann. Phys. **318**, 170 (2005).

[42] H. Chaté, F. Ginelli, G. Grégoire, and F. Raynaud, Collective motion of self-propelled particles interacting without cohesion, Phys. Rev. E **77**, 046113 (2008).

[43] S. Mandal, B. Liebchen, and H. Löwen, Motility-induced Temperature Difference in Coexisting Phases, Phys. Rev. Lett. **123**, 228001 (2019).

[44] J. D. Weeks, D. Chandler, and H. C. Andersen, Role of repulsive forces in determining the equilibrium structure of simple liquids, J. Chem. Phys. **54**, 5237 (1971).

[45] U. M. B. Marconi, L. Caprini, and A. Puglisi, Hydrodynamics of simple active liquids: The emergence of velocity correlations, New J. Phys. **23**, 103024 (2021).

[46] H. H. Wensink and H. Löwen, Emergent states in dense systems of active rods: From swarming to turbulence, J. Phys.: Condens. Matter **24**, 464130 (2012).

[47] J. Dunkel, S. Heidenreich, K. Drescher, H. H. Wensink, M. Bär, and R. E. Goldstein, Fluid Dynamics of Bacterial Turbulence, Phys. Rev. Lett. **110**, 228102 (2013).

[48] D. Nishiguchi and M. Sano, Mesoscopic turbulence and local order in janus particles self-propelling under an ac electric field, Phys. Rev. E **92**, 052309 (2015).

[49] A. Creppy, O. Praud, X. Druart, P. L. Kohnke, and F. Plouraboué, Turbulence of swarming sperm, Phys. Rev. E **92**, 032722 (2015).

[50] P. Guillamat, J. Ignés-Mullol, and F. Sagués, Taming active turbulence with patterned soft interfaces, Nat. Commun. **8**, 564 (2017).

[51] S.-Z. Lin, W.-Y. Zhang, D. Bi, B. Li, and X.-Q. Feng, Energetics of mesoscale cell turbulence in two-dimensional monolayers, Commun. Phys. **4**, 21 (2021).

[52] Z. Liu, W. Zeng, X. Ma, and X. Cheng, Density fluctuations and energy spectra of 3d bacterial suspensions, Soft Matter **17**, 10806 (2021).

[53] K. Qi, E. Westphal, G. Gompper, and R. G. Winkler, Emergence of active turbulence in microswimmer suspensions due to active hydrodynamic stress and volume exclusion, Commun. Phys. **5**, 49 (2022).

[54] R. Alert, J. Casademunt, and J.-F. Joanny, Active turbulence, Annu. Rev. Condens. Matter Phys. **13**, 143 (2022).

[55] A. Onuki, *Phase Transition Dynamics* (Cambridge University Press, Cambridge, UK, 2007).

[56] A. J. Bray, Theory of phase-ordering kinetics, Adv. Phys. **51**, 481 (2002).

[57] H. P. Zhang, A. Be'er, E. L. Florin, and H. L. Swinney, Collective motion and density fluctuations in bacterial colonies, Proc. Natl. Acad. Sci. USA **107**, 13626 (2010).

[58] F. Ginelli, F. Peruani, M. Bär, and H. Chaté, Large-scale Collective Properties of Self-propelled Rods, Phys. Rev. Lett. **104**, 184502 (2010).

[59] F. Peruani, J. Starruß, V. Jakovljevic, L. Søgaard-Andersen, A. Deutsch, and M. Bär, Collective Motion and Nonequilibrium Cluster Formation in Colonies of Gliding Bacteria, Phys. Rev. Lett. **108**, 098102 (2012).

[60] S. Ngo, A. Peshkov, I. S. Aranson, E. Bertin, F. Ginelli, and H. Chaté, Large-scale Chaos and Fluctuations in Active Nematics, Phys. Rev. Lett. **113**, 038302 (2014).

[61] D. Nishiguchi, K. H. Nagai, H. Chaté, and M. Sano, Long-range nematic order and anomalous fluctuations in suspensions of swimming filamentous bacteria, Phys. Rev. E **95**, 020601(R) (2017).

[62] K. Kawaguchi, R. Kageyama, and M. Sano, Topological defects control collective dynamics in neural progenitor cell cultures, Nature (Lond.) **545**, 327 (2017).

[63] B. Mahault, F. Ginelli, and H. Chaté, Quantitative Assessment of the Toner and Theory of Polar Flocks, Phys. Rev. Lett. **123**, 218001 (2019).

[64] J. Iwasawa, D. Nishiguchi, and M. Sano, Algebraic correlations and anomalous fluctuations in ordered flocks of janus particles fueled by an ac electric field, Phys. Rev. Res. **3**, 043104 (2021).

[65] F. Ginelli, The physics of the vicsek model, Eur. Phys. J.: Spec. Top. **225**, 2099 (2016).

[66] D. S. Dean, Langevin equation for the density of a system of interacting langevin processes, J. Phys. A: Math. Gen. **29**, L613 (1996).

[67] T. Nakamura and A. Yoshimori, Derivation of the nonlinear fluctuating hydrodynamic equation from the underdamped langevin equation, J. Phys. A: Math. Theor. **42**, 065001 (2009).

[68] D. Zwillinger, *Table of Integrals, Series, and Products* (Elsevier Science, Amsterdam, 2014).

[69] U. Frisch, *Turbulence: The Legacy of A. N. Kolmogorov* (Cambridge University Press, Cambridge, UK, 1995).

[70] L. Caprini and U. Marini Bettolo Marconi, Active matter at high density: Velocity distribution and kinetic temperature, J. Chem. Phys. **153**, 184901 (2020).

[71] C. Gardiner, *Stochastic Methods: A Handbook for the Natural and Social Sciences* (Springer, Berlin, 2009).

[72] E. Fodor, C. Nardini, M. E. Cates, J. Tailleur, P. Visco, and F. van Wijland, How Far From Equilibrium is Active Matter?, Phys. Rev. Lett. **117**, 038103 (2016).